

# Increasing CO Binding Energy and Defects by Preserving Cu Oxidation State via O<sub>2</sub>-Plasma-Assisted N Doping on CuO Enables High C<sub>2+</sub> Selectivity and Long-Term Stability in Electrochemical CO<sub>2</sub> Reduction

Dong Gyu Park,<sup>◆</sup> Jae Won Choi,<sup>◆</sup> Hoje Chun,<sup>◆</sup> Hae Sung Jang, Heebin Lee, Won Ho Choi, Byeong Cheul Moon, Keon-Han Kim, Min Gyu Kim, Kyung Min Choi,\* Byungchan Han,\* and Jeung Ku Kang\*



Cite This: ACS Catal. 2023, 13, 9222–9233



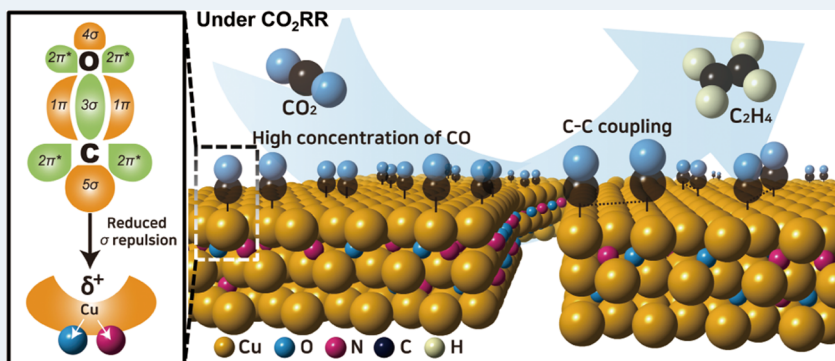
Read Online

ACCESS |

Metrics & More

Article Recommendations

Supporting Information



**ABSTRACT:** Cu is considered as the most promising catalyst for the electrochemical carbon dioxide reduction reaction (CO<sub>2</sub>RR) to produce C<sub>2+</sub> hydrocarbons, but achieving high C<sub>2+</sub> product selectivity and efficiency with long-term stability remains one of great challenges. Herein, we report a strategy to realize the CO<sub>2</sub>RR catalyst allowing high C<sub>2+</sub> product selectivity and stable catalytic properties by utilizing the benefits of oxygen-plasma-assisted nitrogen doping on CuO. It is exhibited that the defects such as oxygen vacancies and grain boundaries suitable for CO<sub>2</sub>RR are generated by N<sub>2</sub> plasma radicals on CuO. Also, the oxidation state of Cu is maintained without Cu reduction by O<sub>2</sub> plasma. Indeed, ON–CuO synthesized through oxygen-plasma-assisted nitrogen doping is demonstrated to enable a high C<sub>2+</sub> product selectivity of 77% (including a high C<sub>2</sub>H<sub>4</sub> selectivity of 56%) with a high current density of  $-34.6\text{ mA/cm}^2$  at  $-1.1\text{ V}$  vs RHE, as well as a long-term stability for 22 h without performance degradation. High CO<sub>2</sub>RR performances are ascribed to the increased CO binding energy and catalytic sites in N-doped CuO. Furthermore, an *in situ* X-ray absorption near-edge structure analysis reveals that the defects in ON–CuO are favorable for C–C coupling leading to C<sub>2+</sub> products.

**KEYWORDS:** electrochemical CO<sub>2</sub> reduction to C<sub>2+</sub> product, O<sub>2</sub>-plasma-assisted N doping, increasing CO binding energy and defect sites, preserving Cu oxidation state, *in situ* X-ray absorption spectroscopy

## INTRODUCTION

There is a growing demand to achieve a sustainable carbon-neutral economy. The electrochemical carbon dioxide reduction reaction (CO<sub>2</sub>RR) produces value-added fuels and feedstock from greenhouse CO<sub>2</sub> gas and reduces the CO<sub>2</sub> footprint; therefore, the reaction has attracted significant attention.<sup>1–7</sup> In particular, multi-carbon (C<sub>2+</sub>) products and oxygenates, such as ethylene (C<sub>2</sub>H<sub>4</sub>) and ethanol (C<sub>2</sub>H<sub>5</sub>OH), are of a great demand because of their high-energy densities and economic and industrial values.<sup>8,9</sup> Among the catalysts used for the CO<sub>2</sub>RR, Cu is the only metal that can catalytically generate C<sub>2+</sub> products.<sup>10–12</sup> However, Cu has a wide distribution of CO<sub>2</sub>RR products, including hydrogen and C<sub>1</sub>

products, thus making the electrosynthesis of the desired C<sub>2+</sub> products challenging.<sup>13–16</sup> Several strategies have been used to tune the structural and chemical properties of Cu-based catalysts, such as the particle size,<sup>17–19</sup> morphology,<sup>20,21</sup> grain boundary,<sup>22–26</sup> roughness,<sup>27,28</sup> and oxidation state,<sup>29–33</sup> to

Received: March 30, 2023

Revised: May 17, 2023

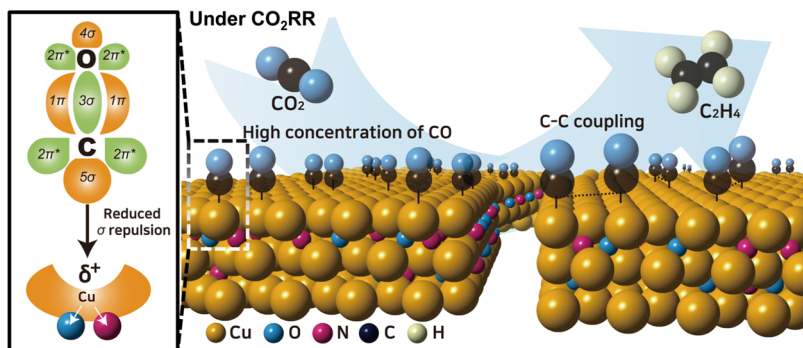


**Figure 1.** Schematic illustration of both increased CO binding energy ascribed to the reduced sigma repulsion and also defect sites favorable for C–C coupling leading to the efficient electrochemical carbon dioxide reduction reaction (CO<sub>2</sub>RR) on ON–CuO synthesized through oxygen-plasma-assisted nitrogen doping.

improve their selectivity for C<sub>2+</sub> products. Tailoring the electronic structure of Cu can promote C–C coupling by optimizing the binding energy between Cu and the CO intermediate, leading to enhanced selectivity for C<sub>2+</sub> products. Also, the electronic structure of Cu can be regulated by creating Cu<sup>δ+</sup> sites on the Cu surface via the oxide-derived Cu (OD-Cu), promoting the electroreduction of carbon dioxide.<sup>12,34–37</sup> Moreover, the increased grain boundaries and undercoordinated Cu sites also play an important role in facilitating C–C coupling.<sup>21,38,39</sup> To obtain high C<sub>2+</sub> selectivity in a Cu-based catalyst for the CO<sub>2</sub>RR, we chose a strategy of changing the bonding environment and the density of the catalytic active site simultaneously. First, to convert CO<sub>2</sub> to C<sub>2+</sub> hydrocarbon products, such as ethylene, the existence of CO as an intermediate product at a high concentration on the catalytic surface is important. Therefore, obtaining appropriate binding energy between CO and Cu is essential. When Cu–CO has a strong binding energy, inducing C–C coupling is difficult. This leads to low C<sub>2+</sub> product selectivity. In contrast, when the Cu–CO binding energy is significantly weak, the selectivity for CO increases, and the amount of C<sub>2+</sub> products is traded off. Furthermore, it is well known that the oxidation state of Cu, which works as the catalytic reaction site, also plays an important role in the C<sub>2+</sub> product pathway. In other words, controlling Cu–CO binding energy while maintaining an appropriate Cu oxidation number is essential. In addition, having many active sites on the catalytic surface is necessary for the reaction. In other words, with many defective sites, the grain boundaries may have high C<sub>2+</sub> product selectivity.

In this work, we show that oxygen-plasma-assisted nitrogen doping on CuO is effective to tune CO binding energy and catalytically active sites for the CO<sub>2</sub>RR, as schematically illustrated in Figure 1. The highly reactive N free radicals of N<sub>2</sub> plasma led to interstitial or substitutional nitrogen atoms in CuO crystals, thereby allowing to modulate the binding energy between Cu and the CO intermediate. We also show that O<sub>2</sub> plasma radicals help to effectively prevent the reduction of Cu by N<sub>2</sub> plasma radicals, thereby allowing to maintain the oxidation state of CuO. Indeed, ON–CuO synthesized through oxygen-plasma-assisted nitrogen doping on CuO is demonstrated to enable high C<sub>2+</sub> product selectivity and long-term stability without performance degradation, which are proven to be ascribed to the increased binding energy between Cu and the CO intermediate owing to the reduced sigma repulsion in nitrogen-doped CuO as well as the additional catalytic reaction sites created by N<sub>2</sub> plasma radicals.

Additionally, an in situ X-ray spectroscopy analysis and density functional theory (DFT) calculations corroborate that the coexistence of N and O in ON–CuO is favorable for C–C coupling leading to the efficient production of C<sub>2+</sub> products.

## RESULTS AND DISCUSSION

CuO nanorods were first synthesized with carbon black as the starting material for plasma treatment. We then performed N<sub>2</sub>, and O<sub>2</sub> and N<sub>2</sub> mixed plasma treatments to elucidate the effect of each plasma on CuO. The surface characteristics of CuO can determine the selectivity of the C<sub>2+</sub> product by modulating the binding energy between the CO intermediate and Cu, which affects C–C coupling during CO<sub>2</sub>RR. We performed the X-ray photoelectron spectroscopy (XPS) of Auger Cu LMM to reveal changes in the oxidation state of the Cu surface in CuO after plasma treatment (Figure 2a). The Cu LMM spectrum of CuO consists of a Cu<sup>2+</sup> peak at 917.7 eV and a Cu<sup>+</sup> peak at 916.3 eV. Compared to the content of Cu<sup>2+</sup>, there was a significantly greater amount of Cu<sup>0</sup> (918.4 eV) and Cu<sup>+</sup> in N–CuO. The spectra of ON–CuO are almost identical to those of CuO, indicating that O<sub>2</sub> plasma serves as an oxygen supplier. A similar trend was also confirmed in high-resolution Cu 2p XPS spectra (Figure S1). Although Cu<sup>+</sup> and Cu<sup>0</sup> are almost indistinguishable in Cu 2p, the difference in the ratio of the Cu<sup>2+</sup> peak to the Cu<sup>+/Cu<sup>0</sup> peak suggests that N–CuO was reduced and ON–CuO maintained its oxidation state. In addition, the X-ray diffraction (XRD) patterns (Figure S2) also indicate that all of the samples were composed of a CuO phase, except for N–CuO with a reduced Cu<sub>2</sub>O phase. To further investigate the chemical state and coordination environment of the plasma-treated CuO, the Cu K-edge X-ray absorption near-edge structure (XANES) and extended X-ray absorption fine structure (EXAFS) measurements were performed. The XANES spectra (Figure S3a) show that CuO and plasma-treated CuO have three peaks at 8985, 8992, and 8997 eV, respectively, similar to those of the CuO reference. Only N–CuO had a small pre-edge peak at 8981 eV, corresponding to Cu<sub>2</sub>O. The Fourier transform (FT) EXAFS spectra showed the main peak corresponding to Cu–O coordination at 1.55 Å (Figure S3b). N<sub>2</sub> plasma treatment drastically reduced the Cu–O peak intensity of N–CuO, and O<sub>2</sub> plasma treatment offset the decrease in the peak intensity of ON–CuO. Furthermore, we defined the coordination environment of Cu by fitting the EXAFS curve (Figure 2b and Table S1). N–CuO had the lowest coordination number of 3.4, whereas ON–CuO had a coordination number of 3.8, analogous to</sup>

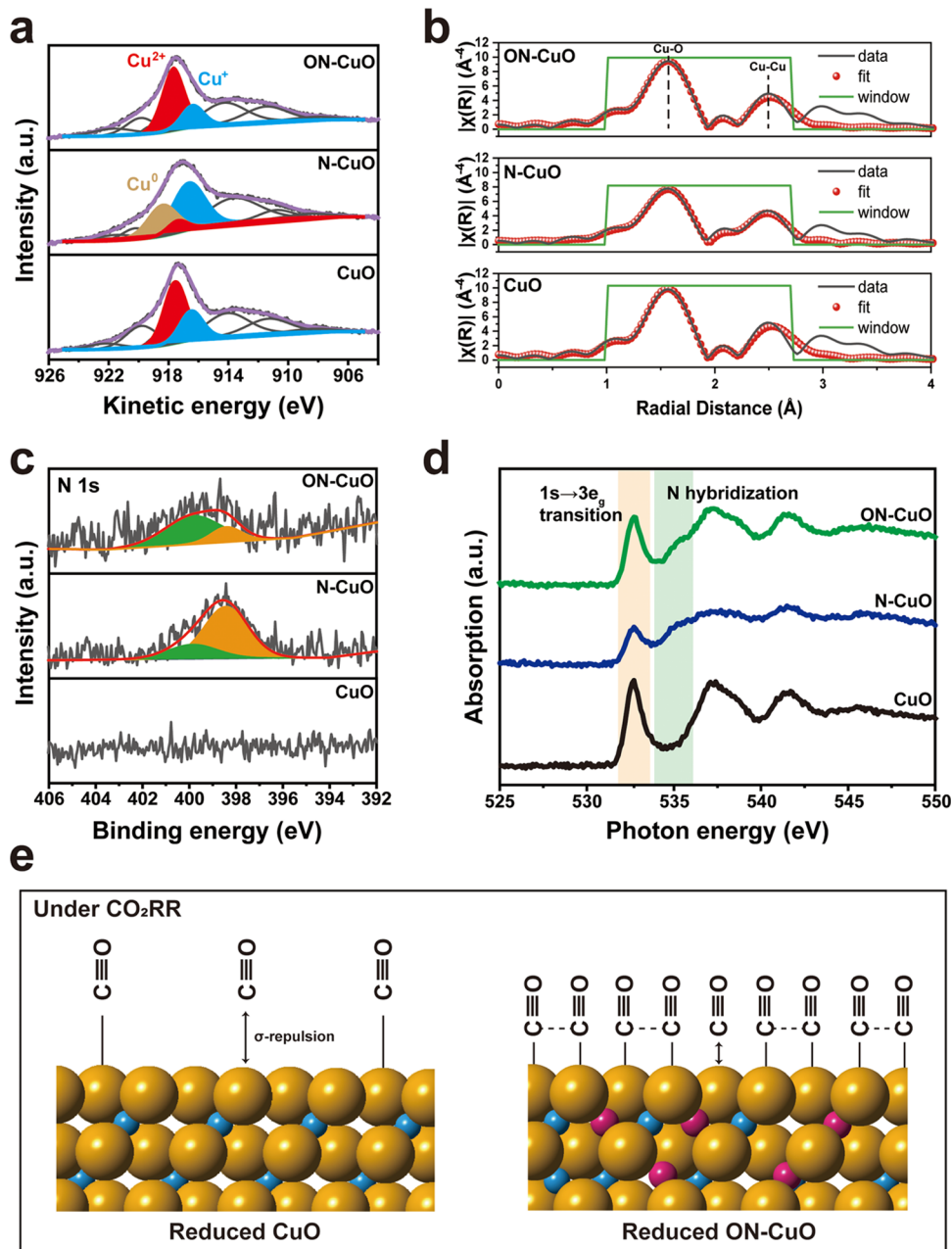


**Figure 2.** Chemical and structural characterizations of ON–CuO. (a) Auger Cu LMM XPS, (b) FT  $k^3$ -weighted Cu K-edge EXAFS fitting, (c) N 1s XPS, and (d) O K-edge NEXAFS spectra of CuO, N–CuO, and ON–CuO. (e) Schematic illustration of the change in the CO intermediate concentration by reducing sigma repulsion.

CuO. The Cu–Cu bond lengths of CuO and ON–CuO were 2.876 and 2.880 Å, respectively. On the other hand, N–CuO has a Cu–Cu bond length of 2.837 Å. These confirm that  $\text{N}_2$  plasma plays a role in breaking Cu–O bonds and forming oxygen vacancy, and  $\text{O}_2$  plasma retains Cu–O bonds. In addition, to examine the existence of nitrogen in nitrogen-doped CuO, the high-resolution XPS spectra of N 1s were measured. As shown in Figure 2c, N 1s spectra were deconvoluted into two characteristic peaks, which were obtained for N–CuO and ON–CuO. The peak at 398 eV corresponds to the N–Cu bond owing to the substitutional doping of nitrogen in the oxygen sites.<sup>40,41</sup> Moreover, the peak at 400 eV indicates the interstitial doping of nitrogen in a CuO lattice, corresponding to Cu–N–O or Cu–O–N bonding. Thus, it can be interpreted that owing to the different

atmospheres of  $\text{N}_2$  and  $\text{O}_2/\text{N}_2$  plasma treatments, nitrogen is doped differently on N–CuO and ON–CuO. In the case of N–CuO, lattice oxygen atoms were dissipated because of the reductive atmosphere of  $\text{N}_2$  plasma, followed by substitutional nitrogen doping on the oxygen vacancy sites. However, the  $\text{N}_2/\text{O}_2$  mixed plasma treatment has a relatively less reductive atmosphere; therefore, oxygen atoms were rarely substituted, and nitrogen was mainly doped interstitially. Through the mixed plasma treatment, nitrogen was interstitially doped while maintaining the oxidation state of Cu. To elucidate whether doped nitrogen can change the electronic structure, the O K-edge NEXAFS analysis was performed (Figure 2d). The O K-edge NEXAFS indirectly provides information of the electronic structure. The characteristic peaks at 532.7, 537.4, 541.5, and 546.2 eV, respectively, were observed. The peak at 532.7 eV

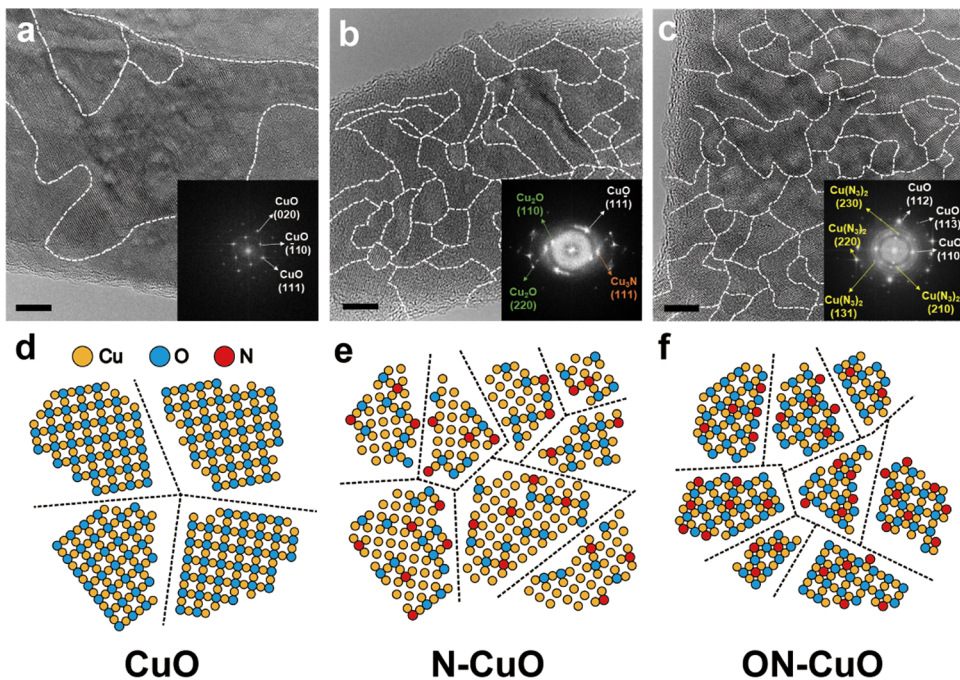


**Figure 3.** Crystal structure and morphology changes in plasma treated samples. TEM images and proposed lattice structures of (a, d) CuO, (b, e) N–CuO, and (c, f) ON–CuO, where the insets of TEM images are the corresponding FFT patterns (scale bar = 5 nm).

corresponds to the 1s → 3e<sub>g</sub> electron transition of CuO, which is generated by the electron transition to the hybridized state of O 2p and Cu 3d.<sup>42</sup> In CuO, the electron configuration of Cu<sup>2+</sup> was partially filled because of the d<sup>9</sup> configuration. The higher energy peaks at 537.4, 541.5, and 546.2 eV result from the electron transition to the hybridized orbital of O (2p and 3p) and Cu (4s and 4p). There was a slight difference in the peak characteristics between each sample. N–CuO exhibited the reduced intensities of the first and second peaks at 532.7 and 537.4 eV, respectively, due to the reduced 1s → 3e<sub>g</sub> transition by the electron configuration of d<sup>10</sup> of Cu<sup>+</sup> or 4s<sup>1</sup> of Cu<sup>0</sup>, which contained more electrons than d<sup>9</sup> of Cu<sup>2+</sup>. The peaks in the higher energy region were also broadened compared to those of pristine CuO, which is attributed to the hybridization of O 2p and Cu (n + 1) sp. This was also the result of additional complex hybridization with Cu (n + 1) sp and N 2p.<sup>42</sup> Similarly, in the case of ON–CuO, Cu was reduced relatively less, and a peak shape similar to that of pristine CuO was observed. However, the second peak of ON–CuO had a shoulder peak in the same low-energy region as that in the case of N–CuO. These different peak characteristics are attributed to additional hybridization with the N 2p orbital, as well as with the O 2p orbital. This confirms that ON–CuO inhibits Cu reduction while being doped with nitrogen to form additional orbitals through the hybridization of the O, N, and Cu orbitals.<sup>43–45</sup> This can lead to a change in Cu–CO binding energy. According to the Blyholder model, the surface bonding of CO and Cu is related to the interplay between the d orbital of Cu and the frontier orbital of CO, which corresponds with the electron donation of the 5-σ orbital (HOMO) and the back-donation of the 2π\* orbital (LUMO), resulting in a sigma bond and a pi bond, respectively.<sup>46</sup> Because the 2π\* orbital is empty and antibonding, electron back-donation weakens C–O internal bonds. When CO molecules are adsorbed on the surface of Cu, depending on the degree of electron back-donation, the length

of the C–Cu bond also changes. Although both the π bond and σ repulsion are affected by the position of the metal d-band, σ repulsion is more affected by the occupancy of the Cu sp orbital. Therefore, the electron acceptor can reduce the σ repulsion by attracting electrons from the Cu sp band.<sup>47</sup> Similarly, copper with subsurface oxygen has been reported to increase the CO binding energy.<sup>34</sup> Through the increased CO binding energy, the concentration of the CO intermediate on the surface kinetically increased the C–C coupling (Figure 2e). In this work, we doped nitrogen into copper oxide using plasma. The doped nitrogen and trapped oxygen on the subsurface make it possible to reduce the σ repulsion. Consequently, it was possible to obtain an improved C<sub>2+</sub> product selectivity compared to that of pristine CuO.

Moreover, more catalytic active sites could be obtained by generating defective sites through nitrogen plasma treatment. We investigated the changes in the crystal structure and morphology of CuO after plasma treatment. No morphological transformation was observed in the scanning electron microscopic (SEM) and low-magnification transmission electron microscopic (TEM) images, as shown in Figures S4 and S5. However, the high-resolution transmission electron microscopic images (Figure 3a–c) show obvious differences in the lattice structure according to the type of plasma treatment. Pristine CuO (Figure 3a,d) has a polycrystalline structure composed of a few grains of the CuO phase, as confirmed by the TEM image and fast Fourier transform (FFT) patterns. On the other hand, as shown in Figure 3b,e, the CuO crystal after N<sub>2</sub> plasma treatment was fragmented, and nitrogen was simultaneously doped on the CuO lattice. The N–CuO crystal attacked by the reactive N radicals was broken, and more grain boundaries were formed. The FFT ring pattern indicates randomly oriented grains, and interestingly, Cu<sub>2</sub>O and Cu<sub>3</sub>N phases were observed, which are based on reduced and nitrogen-doped phases, respectively. This result confirms that N<sub>2</sub> plasma treatment results in nitrogen species on the

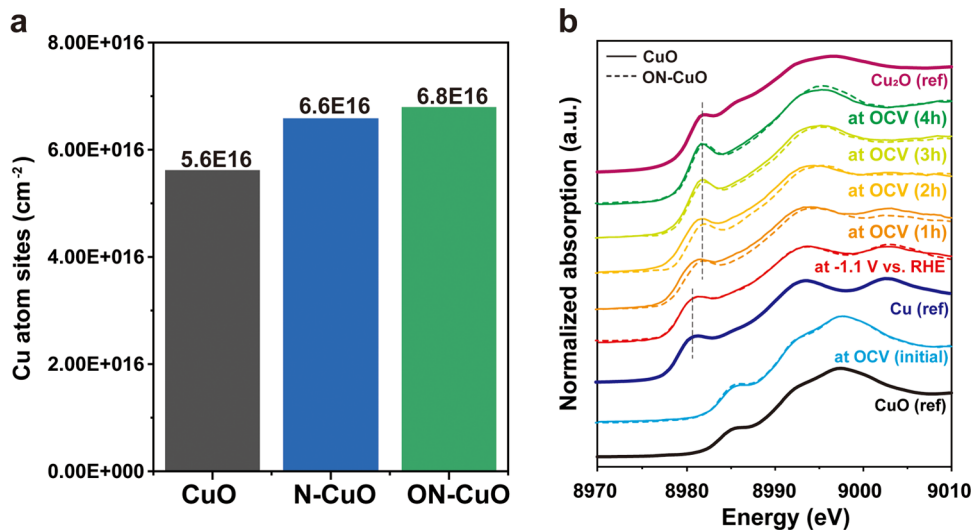


**Figure 4.** Characterizations of the catalytic sites of plasma treated samples. (a) Electrochemical active surface area analysis by Pb underpotential deposition and (b) in situ Cu K-edge XANES analysis of CuO and ON–CuO.

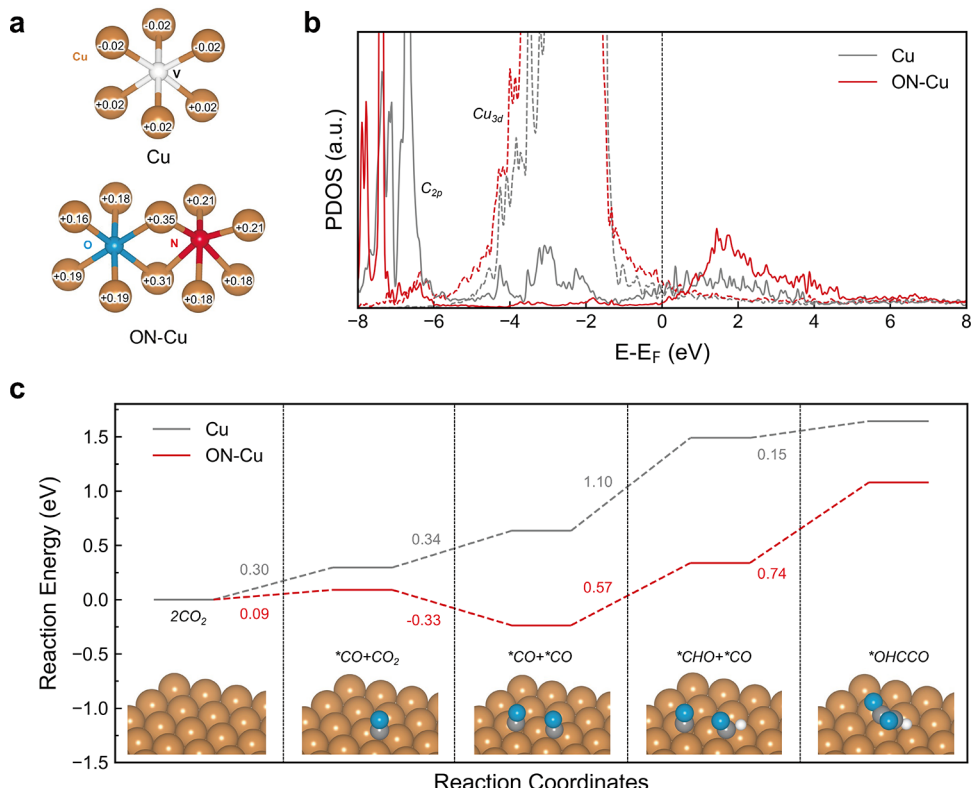


**Figure 5.** DFT calculations on enhancing the formation of  $\text{C}_2^+$  products. (a) Atomic charges on Cu for the bare Cu (111) and ON–Cu surfaces, where V represents the octahedron site in the Cu (111) surface. (b) PDOS of CO-adsorbed surfaces. The dashed lines represent 3d bands for Cu, while the solid lines represent the hybridized 2p orbitals for C. (c) Free-energy diagram of key hydrogenation intermediates to form  $^*\text{OHCCO}$  at  $U = 0$  V.

CuO lattice coupled with the reduction of Cu.  $\text{O}_2/\text{N}_2$ -mixed-plasma-treated CuO (ON–CuO) exhibited significantly different characteristics from those of the pristine samples (Figure 3c,f).  $\text{N}_2$  plasma promoted grain fragmentation and doping of nitrogen atoms on CuO, while  $\text{O}_2$  plasma prevented Cu reduction so that the CuO phase can exist predominantly. The grain size of ON–CuO was significantly reduced, as shown in the TEM image and the ring pattern of the FFT (Figure 3f). In addition, nitrogen was doped in the form of a  $\text{Cu}(\text{N}_3)_2$  phase

with a  $\text{Cu}^{2+}$  valence state, as shown in the FFT pattern, demonstrating suppressed Cu reduction.

Moreover, the electrochemical active surface area (ECSA) analysis was performed to confirm the increase of the catalytic active sites due to the plasma effect (Figure S6). The ECSA analysis was performed by Pb underpotential deposition in an Ar-saturated 0.1 M  $\text{HClO}_4$  with 1 mM  $\text{PbCl}_2$  electrolyte to determine the ECSA of the catalyst (Figure 4a). Compared to pristine CuO, the surface roughness factor increased after the

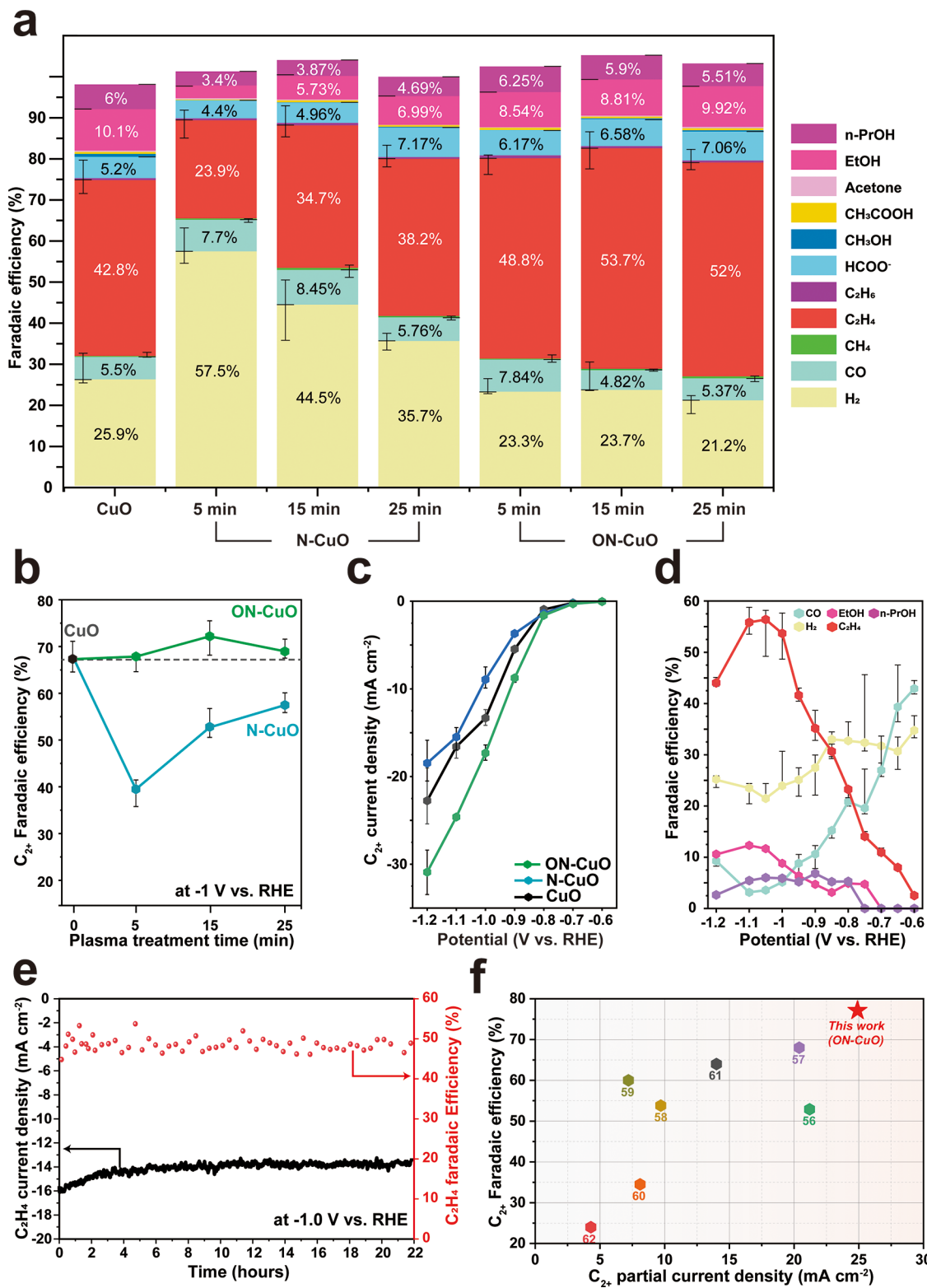


**Figure 6.** Characterizations of CO<sub>2</sub>RR performances in ON–CuO. (a) Faradaic efficiency of different plasma-treated CuO for different products according to the plasma treatment time. (b) Faradaic efficiency for C<sub>2+</sub> products according to the plasma treatment time. (c) Partial current densities of C<sub>2+</sub> products for CuO, N–CuO, and ON–CuO, respectively. (d) Faradaic efficiency of ON–CuO for major products at different potentials. (e) Results of the stability test for ON–CuO at -1.0 V vs RHE for 22 h. (f) Comparison of C<sub>2+</sub> faradaic efficiency and partial current density with previously reported works. The details of the reported results are provided in Table S2.

plasma treatment. ON–CuO exhibited the largest ECSA, which is ascribed to the increase in the number of defective sites and surface roughness, resulting in its largest CO<sub>2</sub>RR

current density.<sup>48,49</sup> We performed an in situ XANES analysis to reveal the origin of the improved faradaic efficiency of the C<sub>2+</sub> products of ON–CuO (Figure 4b). CuO and ON–CuO

showed the same profile as that of CuO reference at the open circuit voltage (OCV) before applying the reduction potential. However, they were reduced to  $\text{Cu}^0$  after the potential was applied at  $-1.1$  V vs RHE for 2 h. Subsequently, the XANES spectra of CuO and ON–CuO were measured at 1 h intervals for 4 h at the OCV. After 1 h, ON–CuO, which was reduced to  $\text{Cu}^0$ , was reoxidized to a  $\text{Cu}_2\text{O}$  phase, while CuO was observed to maintain  $\text{Cu}^0$ . CuO was reoxidized to a  $\text{Cu}_2\text{O}$  phase after 3 h. The defect sites, such as oxygen vacancies and grain boundaries, created by  $\text{O}_2$  and  $\text{N}_2$  plasma improved the surface oxygen mobility,<sup>50</sup> indicating that oxygen is more readily accessed on the surface of ON–CuO than CuO.

To gain atomistic insights into the effects of coordination environments and oxidation states of Cu on the binding strength of CO and  $\text{C}_{2+}$  product formation, we performed the DFT calculations. We modeled  $\text{N}_2$ - and  $\text{O}_2$ -plasma-treated samples as O and N co-doped into the interstitial sites of the Cu (111) surface (ON–Cu) and the reference sample as pristine Cu (111) surface because the surface oxygen atoms are highly likely to be removed under the reducing environments with prolonged reactions (Figure S7). We calculated the projected density of states (PDOS) of the bare surfaces to conjecture the binding affinity toward CO, which is a key intermediate for the formation of  $\text{C}_{2+}$  products (Figure S8). The overall trends of the Cu  $d$ -band are similar to those of bare surfaces, but the  $d$ -band center energy ( $-2.36$  eV) of the ON–Cu surface shifts away from the Fermi level compared to that ( $-2.25$  eV) of the Cu surface. This indicates that Cu atoms in the ON–Cu surface are more positively charged compared to those in the bare surface. As shown in Figure 5a, the atomic charges obtained by Bader charge analysis show that the partial positive charges increased for the ON–Cu surface compared to those of the bare Cu surface. The results reveal that the co-doping of O and N radicals induces the oxidation state of Cu to be  $\text{Cu}^{\delta+}$ . Considering the symmetrically distinct sites in pristine Cu (111) and ON–Cu surfaces, the binding energies of CO were  $-0.93$  and  $-1.13$  eV for the thermodynamically most stable sites on pristine Cu and ON–Cu surfaces, respectively (Table S3). CO is likely to be adsorbed at a face-center crystal site in the bare Cu surface while it is adsorbed at the atop site in between O and N in the subsurface of ON–Cu in which the Cu site becomes reduced by interacting with O and N atoms in the subsurface to attract CO molecules more strongly. As shown in Figure 5b, the PDOS of hybridized  $\text{C}_{2p}$  peaks also reveals that the splitting between bonding and antibonding is larger in the ON–Cu surface compared to that in the Cu (111) surface. The strong binding affinity toward CO in the ON–Cu surface indicates that the reduction reaction to form  $\text{C}_{2+}$  products can be facilitated. To further elucidate the reason for selectivity for  $\text{C}_{2+}$  products, we evaluated the free-energy diagram of key intermediates to form  ${}^*\text{OHCCO}$  as shown in Figure 5c. The formation of  ${}^*\text{CO}$  from  $\text{CO}_2$  (g) undergoes two-electron pathways whose thermodynamic-limiting steps involve in the formation of  ${}^*\text{COOH}$ .<sup>51</sup>  ${}^*\text{CO}$  can have diverged reaction pathways with various reaction intermediates. Previous studies<sup>52–54</sup> showed that the C–C coupling from the  ${}^*\text{CHO}-{}^*\text{CO}$  state is more facile than the direct C–C coupling from  ${}^*\text{CO}-{}^*\text{CO}$ . Hence, we only considered the constrained reaction pathway of C–C coupling forming  ${}^*\text{OHCCO}$  in this work. The overall reaction profile of the ON–Cu surface lies below the pristine one. It is notable that the co-adsorption state of CO ( ${}^*\text{CO}+{}^*\text{CO}$ ) is thermodynamically

stable, which indicates the favorable adsorption of CO leading to the high concentration of the CO intermediate on the surface. Also, the rate-determining step can be attributed to hydrogenation or C–C coupling.<sup>55</sup> The thermodynamic barrier for hydrogenation from  ${}^*\text{CO}$  ( ${}^*\text{CO}+{}^*\text{CO} \rightarrow {}^*\text{CHO} + {}^*\text{CO}$ ) is much lower in the ON–Cu surface than that in the pristine one, thus supporting that the formation of  $\text{C}_{2+}$  products is more favorable to ON–Cu. As a result, the ON–Cu surface facilitates the formation of  $\text{C}_{2+}$  products with the high binding energy of CO as well as the low thermodynamic barriers for hydrogenation and C–C coupling.

We also explored the effect of plasma on CuO via electrochemical  $\text{CO}_2$ RR experiments at  $-1.0$  V vs RHE for various plasma treatment times according to the type of plasma (Figure 6a,b). N–CuO showed a noticeable change in faradaic efficiency. N–CuO, which was plasma-treated for 5 min, showed lower  $\text{C}_{2+}$  and higher  $\text{H}_2$  faradaic efficiency than pristine CuO due to the reductive atmosphere of  $\text{N}_2$  plasma. However, as the plasma treatment time increased, the faradaic efficiency of  $\text{H}_2$  decreased and that of  $\text{C}_{2+}$  products, such as ethylene, increased. This suggests that nitrogen doping can increase the selectivity for the generation of  $\text{C}_{2+}$  products. Nonetheless, when treated with nitrogen plasma alone, Cu was reduced and the oxidation number of Cu approached zero. It is known that Cu shows higher  $\text{C}_{2+}$  selectivity when the oxidation number is positive rather than zero. To confirm the effect of the Cu oxidation state, an electrochemical  $\text{CO}_2$ RR was performed on the sample treated with  $\text{H}_2$  plasma, which is a strong reductive atmosphere (Figures S9–S11). As shown in the results,  $\text{H}_2$ -plasma-treated H–CuO majorly generates  $\text{C}_1$  products, such as formate, rather than  $\text{C}_{2+}$  products, confirming that the reduction of Cu has a negative effect on the formation of  $\text{C}_{2+}$  products. It can be seen that  $\text{C}_{2+}$  selectivity significantly decreases when Cu is excessively reduced. In addition, H–CuO shows invariable faradaic efficiencies despite the increase in the treatment time. We also determined  $\text{CO}_2$ RR with  $\text{O}_2$ -plasma-treated CuO (O–CuO) to clarify the effect of nitrogen doping (Figures S12, S13). Although the oxidation state of CuO was further stabilized by  $\text{O}_2$  plasma treatment, the faradaic efficiencies of O–CuO exhibit no significant change depending on the  $\text{O}_2$  plasma treatment time and the lower  $\text{C}_{2+}$  selectivity compared to those of ON–CuO. These results demonstrate that nitrogen doping through  $\text{N}_2$  plasma treatment improves  $\text{C}_{2+}$  selectivity in electrochemical  $\text{CO}_2$ RR. Therefore,  $\text{O}_2/\text{N}_2$  mixed plasma was treated to obtain N-doped samples while maintaining the oxidation number of Cu appropriately. Considering these findings, the highest  $\text{C}_{2+}$  faradaic efficiency of ON–CuO can be achieved by the synergistic effect of nitrogen doping and the prevention of Cu reduction by the  $\text{O}_2/\text{N}_2$  mixed plasma. The total current densities of plasma-treated CuO were  $-29.3$ ,  $-28.7$ , and  $-34.6$  mA cm $^{-2}$  at  $-1.1$  V vs RHE for CuO, N–CuO, and ON–CuO, respectively (Figure S14). ON–CuO treated with mixed plasma exhibited the largest current density because of the increased number of active sites owing to grain size reduction and nitrogen doping. The total current density of ON–CuO exhibited an increase of 18% compared to pristine CuO. The partial current densities of  $\text{C}_{2+}$  products for CuO, N–CuO, and ON–CuO, were  $-17.8$ ,  $-16.9$ , and  $-24.9$  mA cm $^{-2}$ , respectively (Figure 6c). N–CuO showed slightly smaller values than pristine CuO. This trend is similar to that of the total current density, indicating that treatment with  $\text{N}_2$  plasma alone does not have a significant positive effect on the

electrochemical CO<sub>2</sub>RR. In contrast, the partial current density of the C<sub>2+</sub> product for ON–CuO was increased by 40% compared to that of pristine CuO. This indicates that the mixed plasma treatment, rather than N<sub>2</sub> plasma treatment alone, improves C<sub>2+</sub> product selectivity in the CO<sub>2</sub>RR. It was confirmed that nitrogen doping was possible while maintaining the oxidation number of Cu through the mixed plasma, and that the C<sub>2+</sub> product can be promoted by increasing the number of defective sites and the grain boundary density. Regarding the faradaic efficiency of the product for each voltage of ON–CuO, hydrogen and CO were found to be the major products at a low voltage (Figure 6d). However, as the voltage increases, we found that the generation of hydrogen decreased and that of CO decreased significantly. Moreover, at the same time, the generation of C<sub>2</sub>H<sub>4</sub> was observed to be increased rapidly at −1.1 V (vs RHE) and the faradaic efficiencies of ethylene and the C<sub>2+</sub> product were 56 and 77%, respectively. It can be seen that ON–CuO has an appropriate CO binding energy to create an appropriate environment for generating C<sub>2+</sub> products. We also calculated the turnover frequency (TOF) of C<sub>2</sub>H<sub>4</sub> per Cu atom to prove that high TOF values are mainly not attributed to the surface roughness effect, as confirmed in Figure S15 showing that ON–CuO leads to a higher TOF than pristine CuO. In addition, Tafel slopes in Figure S16 show 132, 119, and 110 mV/dec for CuO, N–CuO, and ON–CuO, respectively. A low Tafel slope indicates a low kinetic barrier and fast electron transfer. From these results, N–CuO and ON–CuO are shown to have a lower kinetic barrier and faster electron transfer for C<sub>2</sub>H<sub>4</sub> formation than pristine CuO, thus explaining the reason for the high C<sub>2</sub>H<sub>4</sub> selectivity of ON–CuO.

A study that employed oxide-derived Cu for electrochemical CO<sub>2</sub>RR reported that if the reaction time is prolonged due to a reducing environment, the oxidation state of Cu is eventually completely reduced to Cu<sup>0</sup> and the catalytic properties deteriorate. Therefore, we investigated the current density and faradaic efficiency of C<sub>2</sub>H<sub>4</sub> generation through an electrochemical CO<sub>2</sub>RR experiment for approximately 22 h (Figure 6e). Consequently, although a slight decrease in the current density occurred during the first few hours, the current remained constant in the subsequent reaction. In addition, it was confirmed that the faradaic efficiency of ethylene production was stable and that the current density and selectivity of the C<sub>2+</sub> product increased when nitrogen was doped through the mixed plasma. Moreover, the catalytic properties were maintained even in a long-term reductive environment without any degradation or aggregation of grains as shown in the TEM images (Figure S17). As shown in the XRD patterns in Figure S18, ON–CuO shows no crystallinity after the stability test. However, it is revealed that most of the nitrogen in ON–CuO was well maintained in the form of interstitial N even after the long-term CO<sub>2</sub>RR (Figure S19). Furthermore, Cu LMM Auger spectra indicate that the surface of ON–CuO is reoxidized to Cu<sup>+</sup>, which is consistent with the FFT pattern of the TEM image in Figure S12 and in situ XANES data. The results of this study were compared with those of previous studies conducted in H-cell-type experiments under neutral electrolyte conditions (Figure 6f).<sup>56–62</sup> As shown in this figure, it was confirmed that the mixed plasma-treated sample conducted in this study showed excellent results not only in C<sub>2+</sub> partial current density but also in faradaic efficiency.

## CONCLUSIONS

In summary, we demonstrated a high-performance CO<sub>2</sub>RR electrocatalyst (ON–CuO) that enables high C<sub>2+</sub> product selectivity and long-term stability. Oxygen-assisted nitrogen doping on CuO was employed to utilize the advantages of oxide-derived CuO and the effect of heteroatom doping. The highly reactive N radicals of N<sub>2</sub> plasma led to interstitial or substitutional nitrogen atoms in CuO crystals, thereby allowing to modulate the binding energy between Cu and the CO intermediate. Also, they resulted in defects such as oxygen vacancies and grain boundaries in CuO. Besides, O<sub>2</sub> plasma radicals effectively prevented the reduction of Cu by N<sub>2</sub> plasma radicals, thereby allowing to maintain the oxidation state of CuO. Moreover, CuO treated with oxygen and nitrogen plasma radicals (ON–CuO) was shown to enable a high C<sub>2+</sub> product selectivity of 77% (including a high C<sub>2</sub>H<sub>4</sub> selectivity of 56%) with a total current density of −34.6 mA/cm<sup>2</sup> at −1.1 V vs RHE, as well as a long-term stability for 22 h. High CO<sub>2</sub>RR performance was ascribed to the increased binding energy between Cu and the CO intermediate owing to the reduced sigma repulsion in nitrogen-doped CuO, as well as the additional catalytic reaction sites created by N<sub>2</sub> plasma radicals. Additionally, an in situ XANES analysis proved that the ON–CuO with defect sites is easily oxidized and favorable for C–C coupling. Consequently, this study supports that modulating CO binding energy and C–C coupling sites through oxygen-plasma-assisted nitrogen doping could pave a route to realize high-performance CO<sub>2</sub>RR catalysts.

## EXPERIMENTAL SECTION

**Synthesis of CuO.** First, 10 mg of Ketjen Black and 170.48 mg of CuCl<sub>2</sub>·2H<sub>2</sub>O (1.0 mmol) were dissolved in a solution mixed with 5 mL of ethanol and 10 mL of distilled water in a 50 mL vial. Then, 880 mg of solid NaOH (22.0 mmol) was dissolved in 25 mL of water in the vial. Subsequently, 25 mL of NaOH aqueous solution was added into the precursor vial. After stirring for 10 min, the precipitate of CuO was obtained. The precipitate was harvested by centrifugation at 8000 rpm for 5 min, washed with distilled water, and then dried at 60 °C in a vacuum oven. Finally, this dried sample was heat-treated in a CVD at 200 °C for 4 h in an Ar atmosphere.

**Plasma Treatment.** The sample was coated on a glass slide and dried in a vacuum oven. Then, the sample was placed in the chamber of the microwave plasma enhanced-chemical vapor deposition equipment. A plasma ball was generated above the sample at a microwave power of 500–600 W, and the plasma had a gas flow of H<sub>2</sub> (99.999%), O<sub>2</sub> (99.999%), N<sub>2</sub> (99.999%), or O<sub>2</sub> and N<sub>2</sub>. The pressure and flow rate of gas were kept constant, and the exposure time to plasma was controlled with a temperature not exceeding 100 °C. After the exposure to the plasma ball, the color of the samples changed based on the type of plasma.

**Material Characterization.** SEM images were taken using a field emission scanning electron microscope (JEM-7600F, JEOL, Japan, SU8230, Hitachi, Japan) operated at 15 kV. TEM images were also obtained by a transmission electron microscope (Tecnai F20, FEI Company, Titan G2, FEI company) at an acceleration voltage of 200 kV. Moreover, powder X-ray diffraction patterns were obtained using an X-ray diffractometer (Smartlab, Rigaku, Japan) with a Cu K $\alpha$  radiation source at 1200 W (40 kV, 30 mA). X-ray photoelectron spectroscopy spectra were also obtained using

an X-ray photoelectron spectroscope (K- $\alpha$ , Thermo Scientific) with an Al-K $\alpha$  radiation at a beam current of 3 mA and a beam size of 0.4 mm. X-ray absorption spectroscopy including XANES and the EXAFS were conducted at a multipole-wiggler 10C beamline, and NEXAFS measurement was performed at the 4D beam line at the Pohang Accelerator Laboratory (PAL). The synchrotron radiations were monochromatized using a Si (111) double-crystal monochromator. The incident beams were detuned with proper rates for harmonic rejection. The Cu K-edge spectra obtained in the transmission mode were analyzed using Athena and Artemis software from the IFEFFIT library.

**Characterization of the Electrochemical CO<sub>2</sub>RR.** The catalyst was coated on a glassy carbon substrate, which was then used as a cathode for electroreduction of CO<sub>2</sub> in a 0.1 M KHCO<sub>3</sub> solution. The electrolyte was first purged with CO<sub>2</sub> to attain a pH of 6.8. Electrochemical measurements were conducted using a Biologic SP-300 potentiostat. CO<sub>2</sub> electrolysis was performed in a custom-made H-type electrochemical cell, in which the working electrode is parallel to the counter electrode and the geometric area for the working electrodes was 0.2 cm<sup>2</sup>. The average mass loading of samples on the working electrode is 300  $\mu$ g cm<sup>-2</sup>. In order to separate the anodic and cathodic chambers, a Selemion AMVN anion-exchange membrane was used. The electrolyte of the cathodic compartment was saturated with CO<sub>2</sub> for at least 15 min prior to conducting electrolysis. CO<sub>2</sub> was sparged during the electrolysis at a flow rate of 20 sccm. A platinum mesh and a Ag/AgCl electrode (leak free series) were used as the counter electrode and the reference electrode, respectively. Pt mesh has a high surface area not to limit current of the working electrode. All collected data were rescaled to the RHE using the following equation

$$E \text{ vs RHE} = E \text{ vs Ag/AgCl} + 0.197 \text{ V} + 0.0591 \times \text{pH} \quad (1)$$

The solution and charge transfer resistances were measured using electrochemical impedance spectroscopy by scanning from 1 MHz to 10 Hz prior to the electrolysis and all reported CVs and electrolysis measurements were made 95% IR-compensated. The ECSA of a catalyst was estimated from Pb underpotential method.

$$\Delta J_{\text{non-faradaic}} = (J_{\text{anodic}} - J_{\text{cathodic}}) = \nu \cdot C_{\text{dl}} \quad (2)$$

**Electrochemical Surface Area.** Pb underpotential deposition (UPD) method was used following previous studies.<sup>63–65</sup> The electrolyte of 0.1 M HClO<sub>4</sub> and 1 mM PbCl<sub>2</sub> aqueous solution (pH 1.54) was purged with Ar gas. Cyclic voltammetry was measured from -0.1 to -0.5 V vs the Ag/AgCl reference electrode at a scan rate of 10 mV/s.

**Product Analysis.** Gaseous products were analyzed with a gas chromatograph (Young Lin instruments) equipped with a packed Porapak Q column, a packed MolSieve 5A column, and a capillary Gaspro column. CO, CH<sub>4</sub>, C<sub>2</sub>H<sub>4</sub>, and C<sub>2</sub>H<sub>6</sub> were detected using a flame ionization detector (FID) with a methanizer in He as the carrier gas. H<sub>2</sub> was analyzed using a thermal conductivity detector (TCD) in argon carrier gas. Calibration of the gas chromatograph was performed using a calibration gas with various concentrations. Online gas product analysis was carried out every 25 min by flowing CO<sub>2</sub> directly into the gas-sampling loop of the gas chromatograph during 1.6 h electrolysis. Faradaic efficiencies were obtained by averaging the individual product analysis. Liquid products were

collected from the cathodic compartments after electrolysis and subsequently analyzed by <sup>1</sup>H-NMR (Bruker AVANCE III HD, 9.4T) equipped with a 400 MHz 5 mm BBFO probe with z-gradients. Topspin software was used for spectrometer control. MestreNova software was used for the quantitative analysis to obtain faradaic efficiency.

**First-Principles Calculations.** All DFT calculations were performed with Vienna Ab-initio Simulation Package (VASP) with the revised Perdew-Burke Ernzerhof (RPBE)<sup>66</sup> generalized gradient approximation (GGA) exchange-correlation functional. The projector-augmented-wave (PAW) basis set<sup>67</sup> with a cutoff energy of 520 eV was used to consider core-electron interaction. Spin polarization and van der Waals (vdW) interaction with the DFT-D3 method by Grimme<sup>68</sup> were considered for all calculations. Slab models of 5 atomic layers, of which 2 atomic layers were fixed, were constructed with a 3 × 3 × 1 supercell and a 15 Å vacuum space. All surfaces were optimized until the total energy and forces were converged within 10<sup>-4</sup> and 0.02 eV Å<sup>-1</sup>, respectively. A Γ-centered 3 × 3 × 1 k-point grid was used for geometry optimization, and a 9 × 9 × 1 k-point grid was used for the electronic structure calculations. More details about the model systems and reaction free energy diagram can be found in Supporting Information.

## ASSOCIATED CONTENT

### Supporting Information

The Supporting Information is available free of charge at <https://pubs.acs.org/doi/10.1021/acscatal.3c01441>.

Method details; characterization details; computational details; XPS spectra; SEM images; TEM images; XRD spectra; XANES spectra; cyclic voltammograms; faradaic efficiency; current density; TOF analysis; Tafel plot; projected density of states; EXAFS fitting parameter table; previously reported results table; CO adsorption energy table; ZPE-TS correction table ([PDF](#))

Web Enhanced Object Figure 1 ([TIF](#))

Web Enhanced Object Figure 2 ([TIF](#))

Web Enhanced Object Figure 3 ([TIF](#))

Web Enhanced Object Figure 4 ([TIF](#))

Web Enhanced Object Figure 5 ([TIF](#))

Web Enhanced Object Figure 6 ([TIF](#))

## AUTHOR INFORMATION

### Corresponding Authors

Kyung Min Choi – Department of Chemical and Biological Engineering, Sookmyung Women's University, Seoul 04310, Republic of Korea;  [orcid.org/0000-0001-7181-902X](https://orcid.org/0000-0001-7181-902X); Email: [kmchoi@sm.ac.kr](mailto:kmchoi@sm.ac.kr)

Byungchan Han – Department of Chemical and Biomolecular Engineering, Yonsei University, Seoul 03722, Republic of Korea;  [orcid.org/0000-0002-2325-6733](https://orcid.org/0000-0002-2325-6733); Email: [bchan@yonsei.ac.kr](mailto:bchan@yonsei.ac.kr)

Jeung Ku Kang – Department of Materials Science and Engineering, KAIST, Daejeon 34141, Republic of Korea;  [orcid.org/0000-0003-3409-7544](https://orcid.org/0000-0003-3409-7544); Email: [jeungku@kaist.ac.kr](mailto:jeungku@kaist.ac.kr)

### Authors

Dong Gyu Park – Department of Materials Science and Engineering, KAIST, Daejeon 34141, Republic of Korea

Jae Won Choi – Materials Architecturing Research Center, Korea Institute of Science and Technology (KIST), Seoul 02792, Republic of Korea

Hoje Chun – Department of Chemical and Biomolecular Engineering, Yonsei University, Seoul 03722, Republic of Korea; [orcid.org/0000-0003-0624-536X](https://orcid.org/0000-0003-0624-536X)

Hae Sung Jang – PLS-II Beamline Division, PLS-II Department, Pohang Accelerator Laboratory (PAL), Pohang University of Science and Technology (POSTECH), Pohang, Gyeongsbuk 37673, Republic of Korea

Heebin Lee – Department of Materials Science and Engineering, KAIST, Daejeon 34141, Republic of Korea

Won Ho Choi – Department of Chemistry, Massachusetts Institute of Technology, Cambridge, Massachusetts 02139, United States

Byeong Cheul Moon – Clean Energy Research Center, Korea Institute of Science and Technology (KIST), Seoul 02792, Republic of Korea

Keon-Han Kim – Department of Chemistry, University of Oxford, Oxford OX1 3TA, United Kingdom

Min Gyu Kim – PLS-II Beamline Division, PLS-II Department, Pohang Accelerator Laboratory (PAL), Pohang University of Science and Technology (POSTECH), Pohang, Gyeongsbuk 37673, Republic of Korea; [orcid.org/0000-0002-2366-6898](https://orcid.org/0000-0002-2366-6898)

Complete contact information is available at:  
<https://pubs.acs.org/10.1021/acscatal.3c01441>

## Author Contributions

◆D.G.P., J.W.C. and H.C. contributed equally to this work. D.G.P.: Conceptualization, writing-original draft, visualization, investigation, project administration; J.W.C.: Conceptualization, writing-original draft, visualization, investigation; H.C.: Investigation, visualization, writing-original draft; H.S.J.: Investigation; H.L.: Resources; W.H.C.: Resources; B.C.M.: Resources; K-H.K.: Resources; M.G.K.: Investigation; B.H.: Writing-review & editing; K.M.C.: Writing-review & editing; and J.K.K.: Supervision, Writing-review & editing. The manuscript was written through contributions of all authors. All authors have given approval to the final version of the manuscript.

## Notes

The authors declare no competing financial interest.

## ACKNOWLEDGMENTS

This research was mainly supported by the National Research Foundation of Korea (2022M3H4A1A04096482, RS-2023-00229679) funded by the Ministry of Science and ICT.

## REFERENCES

- (1) Dorner, R. W.; Hardy, D. R.; Williams, F. W.; Willauer, H. D. Heterogeneous Catalytic CO<sub>2</sub> Conversion to Value-Added Hydrocarbons. *Energy Environ. Sci.* **2010**, *3*, 884–890.
- (2) Liu, M.; Yi, Y.; Wang, L.; Guo, H.; Bogaerts, A. Hydrogenation of Carbon Dioxide to Value-Added Chemicals by Heterogeneous Catalysis and Plasma Catalysis. *Catalysts* **2019**, *9*, 275.
- (3) Bushuyev, O. S.; de Luna, P.; Dinh, C. T.; Tao, L.; Saur, G.; van de Lagemaat, J.; Kelley, S. O.; Sargent, E. H. What Should We Make with CO<sub>2</sub> and How Can We Make It? *Joule* **2018**, *2*, 825–832.
- (4) Liu, W.; Feng, J.; Wei, T.; Liu, Q.; Zhang, S.; Luo, Y.; Luo, J.; Liu, X. Active-Site and Interface Engineering of Cathode Materials for Aqueous Zn—Gas Batteries. *Nano Res.* **2023**, *16*, 2325–2346.
- (5) Gao, S.; Wei, T.; Sun, J.; Liu, Q.; Ma, D.; Liu, W.; Zhang, S.; Luo, J.; Liu, X. Atomically Dispersed Metal-Based Catalysts for Zn—CO<sub>2</sub> Batteries. *Small Struct.* **2022**, *3*, No. 2200086.
- (6) Gao, S.; Wang, T.; Jin, M.; Zhang, S.; Liu, Q.; Hu, G.; Yang, H.; Luo, J.; Liu, X. Bifunctional Nb-N-C Atomic Catalyst for Aqueous Zn-Air Battery Driving CO<sub>2</sub> Electrolysis. *Sci. China Mater.* **2023**, *66*, 1013–1023.
- (7) Wang, X.; Liu, S.; Zhang, H.; Zhang, S.; Meng, G.; Liu, Q.; Sun, Z.; Luo, J.; Liu, X. Polycrystalline SnS<sub>x</sub> Nanofilm Enables CO<sub>2</sub> Electroreduction to Formate with High Current Density. *Chem. Commun.* **2022**, *58*, 7654–7657.
- (8) Hill, J.; Nelson, E.; Tilman, D.; Polasky, S.; Tiffany, D. Environmental, Economic, and Energetic Costs and Benefits of Biodiesel and Ethanol Biofuels. *Proc. Natl. Acad. Sci. U.S.A.* **2006**, *103*, 11206–112.
- (9) Farrell, A. E.; Plevin, R. J.; Turner, B. T.; Jones, A. D.; O'Hare, M.; Kammen, D. M. Ethanol Can Contribute to Energy and Environmental Goals. *Science* **2006**, *311*, 506–508.
- (10) Gao, D.; Arán-Ais, R. M.; Jeon, H. S.; Roldan Cuenya, B. Rational Catalyst and Electrolyte Design for CO<sub>2</sub> Electroreduction towards Multicarbon Products. *Nat. Catal.* **2019**, *2*, 198–210.
- (11) Fan, Q.; Zhang, X.; Ge, X.; Bai, L.; He, D.; Qu, Y.; Kong, C.; Bi, J.; Ding, D.; Cao, Y.; Duan, X.; Wang, J.; Yang, J.; Wu, Y. Manipulating Cu Nanoparticle Surface Oxidation States Tunes Catalytic Selectivity toward CH<sub>4</sub> or C<sub>2+</sub> Products in CO<sub>2</sub> Electroreduction. *Adv. Energy Mater.* **2021**, *11*, No. 2101424.
- (12) Lee, S. H.; Lin, J. C.; Farmand, M.; Landers, A. T.; Feaster, J. T.; Avilés Acosta, J. E.; Beaman, J. W.; Ye, Y.; Yano, J.; Mehta, A.; Davis, R. C.; Jaramillo, T. F.; Hahn, C.; Drisdell, W. S. Oxidation State and Surface Reconstruction of Cu under CO<sub>2</sub> Reduction Conditions from in Situ X-Ray Characterization. *J. Am. Chem. Soc.* **2021**, *143*, 588–592.
- (13) Li, F.; Thevenon, A.; Rosas-Hernández, A.; Wang, Z.; Li, Y.; Gabardo, C. M.; Ozden, A.; Dinh, C. T.; Li, J.; Wang, Y.; Edwards, J. P.; Xu, Y.; McCallum, C.; Tao, L.; Liang, Z. Q.; Luo, M.; Wang, X.; Li, H.; O'Brien, C. P.; Tan, C. S.; Nam, D. H.; Quintero-Bermudez, R.; Zhuang, T. T.; Li, Y. C.; Han, Z.; Britt, R. D.; Sinton, D.; Agapie, T.; Peters, J. C.; Sargent, E. H. Molecular Tuning of CO<sub>2</sub>-to-Ethylene Conversion. *Nature* **2020**, *577*, 509–513.
- (14) Möller, T.; Scholten, F.; Thanh, T. N.; Sinev, I.; Timoshenko, J.; Wang, X.; Jovanov, Z.; Gleich, M.; Roldan Cuenya, B.; Varela, A. S.; Strasser, P. Electrocatalytic CO<sub>2</sub> Reduction on CuO<sub>x</sub> Nanocubes: Tracking the Evolution of Chemical State, Geometric Structure, and Catalytic Selectivity Using Operando Spectroscopy. *Angew. Chem., Int. Ed.* **2020**, *59*, 17974–17983.
- (15) Nitopi, S.; Bertheussen, E.; Scott, S. B.; Liu, X.; Engstfeld, A. K.; Horch, S.; Seger, B.; Stephens, I. E. L.; Chan, K.; Hahn, C.; Nørskov, J. K.; Jaramillo, T. F.; Chorkendorff, I. Progress and Perspectives of Electrochemical CO<sub>2</sub> Reduction on Copper in Aqueous Electrolyte. *Chem. Rev.* **2019**, *119*, 7610–7672.
- (16) Todorova, T. K.; Schreiber, M. W.; Fontecave, M. Mechanistic Understanding of CO<sub>2</sub> Reduction Reaction (CO<sub>2</sub>RR) Toward Multicarbon Products by Heterogeneous Copper-Based Catalysts. *ACS Catal.* **2020**, *10*, 1754–1768.
- (17) Kim, D.; Kley, C. S.; Li, Y.; Yang, P. Copper Nanoparticle Ensembles for Selective Electroreduction of CO<sub>2</sub> to C<sub>2</sub>–C<sub>3</sub> Products. *Proc. Natl. Acad. Sci. U.S.A.* **2017**, *114*, 10560–10565.
- (18) Choi, C.; Cheng, T.; Flores Espinosa, M.; Fei, H.; Duan, X.; Goddard, W. A., III; Huang, Y. A Highly Active Star Decahedron Cu Nanocatalyst for Hydrocarbon Production at Low Overpotentials. *Adv. Mater.* **2019**, *31*, No. 1805405.
- (19) Mi, Y.; Peng, X.; Liu, X.; Luo, J. Selective Formation of C<sub>2</sub> Products from Electrochemical CO<sub>2</sub> Reduction over Cu<sub>1.8</sub>Se Nano-wires. *ACS Appl. Energy Mater.* **2018**, *1*, 5119–5123.
- (20) de Luna, P.; Quintero-Bermudez, R.; DInh, C. T.; Ross, M. B.; Bushuyev, O. S.; Todorović, P.; Regier, T.; Kelley, S. O.; Yang, P.; Sargent, E. H. Catalyst Electro-Redeposition Controls Morphology and Oxidation State for Selective Carbon Dioxide Reduction. *Nat. Catal.* **2018**, *1*, 103–110.

- (21) Wang, X.; Klingan, K.; Klingenhof, M.; Möller, T.; Ferreira de Araújo, J.; Martens, I.; Bagger, A.; Jiang, S.; Rossmeisl, J.; Dau, H.; Strasser, P. Morphology and Mechanism of Highly Selective Cu (II) Oxide Nanosheet Catalysts for Carbon Dioxide Electroreduction. *Nat. Commun.* **2021**, *12*, No. 794.
- (22) Chen, Z.; Wang, T.; Liu, B.; Cheng, D.; Hu, C.; Zhang, G.; Zhu, W.; Wang, H.; Zhao, Z. J.; Gong, J. Grain-Boundary-Rich Copper for Efficient Solar-Driven Electrochemical CO<sub>2</sub> Reduction to Ethylene and Ethanol. *J. Am. Chem. Soc.* **2020**, *142*, 6878–6883.
- (23) Feng, X.; Jiang, K.; Fan, S.; Kanan, M. W. Grain-Boundary-Dependent CO<sub>2</sub> Electroreduction Activity. *J. Am. Chem. Soc.* **2015**, *137*, 4606–4609.
- (24) Li, C. W.; Ciston, J.; Kanan, M. W. Electroreduction of Carbon Monoxide to Liquid Fuel on Oxide-Derived Nanocrystalline Copper. *Nature* **2014**, *508*, 504–507.
- (25) Gu, Z.; Shen, H.; Chen, Z.; Yang, Y.; Yang, C.; Ji, Y.; Wang, Y.; Zhu, C.; Liu, J.; Li, J.; Sham, T. K.; Xu, X.; Zheng, G. Efficient Electrocatalytic CO<sub>2</sub> Reduction to C<sub>2+</sub> Alcohols at Defect-Site-Rich Cu Surface. *Joule* **2021**, *5*, 429–440.
- (26) Mi, Y.; Shen, S.; Peng, X.; Bao, H.; Liu, X.; Luo, J. Selective Electroreduction of CO<sub>2</sub> to C<sub>2</sub> Products over Cu<sub>3</sub>N-Derived Cu Nanowires. *ChemElectroChem* **2019**, *6*, 2393–2397.
- (27) Tang, W.; Peterson, A. A.; Varela, A. S.; Jovanov, Z. P.; Bech, L.; Durand, W. J.; Dahl, S.; Nørskov, J. K.; Chorkendorff, I. The Importance of Surface Morphology in Controlling the Selectivity of Polycrystalline Copper for CO<sub>2</sub> Electroreduction. *Phys. Chem. Chem. Phys.* **2012**, *14*, 76–81.
- (28) Jiang, K.; Huang, Y.; Zeng, G.; Toma, F. M.; Goddard, W. A.; Bell, A. T. Effects of Surface Roughness on the Electrochemical Reduction of CO<sub>2</sub> over Cu. *ACS Energy Lett.* **2020**, *5*, 1206–1214.
- (29) Xiao, H.; Goddard, W. A.; Cheng, T.; Liu, Y. Cu Metal Embedded in Oxidized Matrix Catalyst to Promote CO<sub>2</sub> Activation and CO Dimerization for Electrochemical Reduction of CO<sub>2</sub>. *Proc. Natl. Acad. Sci. U.S.A.* **2017**, *114*, 6685–6688.
- (30) Favaro, M.; Xiao, H.; Cheng, T.; Goddard, W. A., III.; Yano, J.; Crumlin, E. J. Subsurface Oxide Plays a Critical Role in CO<sub>2</sub> Activation by Cu (111) Surfaces to Form Chemisorbed CO<sub>2</sub>, the First Step in Reduction of CO<sub>2</sub>. *Proc. Natl. Acad. Sci. U.S.A.* **2017**, *114*, 6706–6711.
- (31) Liu, G.; Adesina, P.; Nasiri, N.; Wang, H.; Sheng, Y.; Wu, S.; Kraft, M.; Lapkin, A. A.; Ager, J. W.; Xu, R. Elucidating Reaction Pathways of the CO<sub>2</sub> Electroreduction via Tailorable Tortuosities and Oxidation States of Cu Nanostructures. *Adv. Funct. Mater.* **2022**, *32*, No. 2204993.
- (32) Wan, L.; Zhou, Q.; Wang, X.; Wood, T. E.; Wang, L.; Duchesne, P. N.; Guo, J.; Yan, X.; Xia, M.; Li, Y. F.; Jelle, A. A.; Ulmer, U.; Jia, J.; Li, T.; Sun, W.; Ozin, G. A. Cu<sub>2</sub>O Nanocubes with Mixed Oxidation-State Facets for (Photo)Catalytic Hydrogenation of Carbon Dioxide. *Nat. Catal.* **2019**, *2*, 889–898.
- (33) Wei, T.; Zhang, S.; Liu, Q.; Qiu, Y.; Luo, J.; Liu, X. Oxygen Vacancy-Rich Amorphous Copper Oxide Enables Highly Selective Electroreduction of Carbon Dioxide to Ethylene. *Acta Phys. - Chim. Sin.* **2023**, *39*, 220726-0.
- (34) Eilert, A.; Cavalca, F.; Roberts, F. S.; Osterwalder, J.; Liu, C.; Favaro, M.; Crumlin, E. J.; Ogasawara, H.; Friebel, D.; Pettersson, L. G. M.; Nilsson, A. Subsurface Oxygen in Oxide-Derived Copper Electrocatalysts for Carbon Dioxide Reduction. *J. Phys. Chem. Lett.* **2017**, *8*, 285–290.
- (35) Wang, H. Y.; Soldemo, M.; Degerman, D.; Lömkner, P.; Schlueter, C.; Nilsson, A.; Amann, P. Direct Evidence of Subsurface Oxygen Formation in Oxide-Derived Cu by X-Ray Photoelectron Spectroscopy. *Angew. Chem., Int. Ed.* **2022**, *61*, No. e202111021.
- (36) Pardo Pérez, L. C.; Arndt, A.; Stojkovikj, S.; Ahmet, I. Y.; Arens, J. T.; Dattila, F.; Wendt, R.; Guilherme Buzanich, A.; Radtke, M.; Davies, V.; Höflich, K.; Köhnen, E.; Tockhorn, P.; Golnak, R.; Xiao, J.; Schuck, G.; Wöllgarten, M.; López, N.; Mayer, M. T. Determining Structure-Activity Relationships in Oxide Derived Cu-Sn Catalysts During CO<sub>2</sub> Electroreduction Using X-Ray Spectroscopy. *Adv. Energy Mater.* **2022**, *12*, No. 2103328.
- (37) Wei, T.; Zhang, S.; Liu, Q.; Qiu, Y.; Luo, J.; Liu, X. Oxygen Vacancy-Rich Amorphous Copper Oxide Enables Highly Selective Electroreduction of Carbon Dioxide to Ethylene. *Acta Phys. - Chim. Sin.* **2023**, *39*, 1–9.
- (38) Lu, X. K.; Lu, B.; Li, H.; Lim, K.; Seitz, L. C. Stabilization of Undercoordinated Cu Sites in Strontium Copper Oxides for Enhanced Formation of C<sub>2+</sub> Products in Electrochemical CO<sub>2</sub> Reduction. *ACS Catal.* **2022**, *12*, 6663–6671.
- (39) Jun, M.; Kwak, C.; Lee, S. Y.; Joo, J.; Kim, J. M.; Im, J.; Cho, M. K.; Baik, H.; Hwang, Y. J.; Kim, H.; Lee, K.; Jun, M.; Kwak, C.; Joo, J.; Kim, H.; Lee, K.; Lee, S. Y.; Kim, J. M.; Hwang, Y. J.; Im, D. J.; Cho, M. K. Microfluidics-Assisted Synthesis of Hierarchical Cu<sub>2</sub>O Nanocrystal as C<sub>2</sub>-Selective CO<sub>2</sub> Reduction Electrocatalyst. *Small Methods* **2022**, *6*, No. 2200074.
- (40) Wang, Z.; Xu, L.; Huang, F.; Qu, L.; Li, J.; Asare Owusu, K.; Liu, Z.; Lin, Z.; Xiang, B.; Liu, X.; Zhao, K.; Liao, X.; Yang, W.; Cheng, Y.-B.; Mai, L.; Wang, Z. Y.; Xu, L.; Huang, F. Z.; Li, J. T.; Owusu, K. A.; Liu, Z. A.; Lin, Z. F.; Xiang, B. H.; Liu, X.; Zhao, K. N.; Yang, W.; Cheng, Y.; Mai, L. Q.; Qu, L. B.; Liao, X. B. Copper-Nickel Nitride Nanosheets as Efficient Bifunctional Catalysts for Hydrazine-Assisted Electrolytic Hydrogen Production. *Adv. Energy Mater.* **2019**, *9*, No. 1900390.
- (41) He, T.; Zeng, X.; Rong, S. The Controllable Synthesis of Substitutional and Interstitial Nitrogen-Doped Manganese Dioxide: The Effects of Doping Sites on Enhancing the Catalytic Activity. *J. Mater. Chem. A* **2020**, *8*, 8383–8396.
- (42) Sharma, A.; Varshney, M.; Ha, T. K.; Chae, K. H.; Shin, H. J. X-Ray Absorption Spectroscopy Study and Photocatalyst Application of CuO and Cu<sub>0.9</sub>Ti<sub>0.1</sub>O Nanoparticles. *Curr. Appl. Phys.* **2015**, *15*, 1148–1155.
- (43) Kang, L.; Wang, B.; Bing, Q.; Zalibera, M.; Büchel, R.; Xu, R.; Wang, Q.; Liu, Y.; Gianolio, D.; Tang, C. C.; Gibson, E. K.; Danaie, M.; Allen, C.; Wu, K.; Marlow, S.; Sun, L. d.; He, Q.; Guan, S.; Savitsky, A.; Velasco-Vélez, J. J.; Callison, J.; Kay, C. W. M.; Pratsinis, S. E.; Lubitz, W.; Liu, J.-y.; Wang, F. R. Adsorption and Activation of Molecular Oxygen over Atomic Copper(I/II) Site on Ceria. *Nat. Commun.* **2020**, *11*, No. 4008.
- (44) Jin, H.; Liu, X.; Chen, S.; Vasileff, A.; Li, L.; Jiao, Y.; Song, L.; Zheng, Y.; Qiao, S. Z. Heteroatom-Doped Transition Metal Electrocatalysts for Hydrogen Evolution Reaction. *ACS Energy Lett.* **2019**, *4*, 805–810.
- (45) Zhou, Y.; Che, F.; Liu, M.; Zou, C.; Liang, Z.; de Luna, P.; Yuan, H.; Li, J.; Wang, Z.; Xie, H.; Li, H.; Chen, P.; Bladt, E.; Quintero-Bermudez, R.; Sham, T. K.; Bals, S.; Hofkens, J.; Sinton, D.; Chen, G.; Sargent, E. H. Dopant-Induced Electron Localization Drives CO<sub>2</sub> Reduction to C<sub>2</sub> Hydrocarbons. *Nat. Chem.* **2018**, *10*, 974–980.
- (46) Blyholder, G. Molecular Orbital View of Chemisorbed Carbon Monoxide. *J. Phys. Chem. A* **1964**, *68*, 2772–2778.
- (47) Li, B.; Gao, W.; Jiang, Q. Electronic and Geometric Determinants of Adsorption: Fundamentals and Applications. *J. Phys.: Energy* **2021**, *3*, No. 022001.
- (48) Wang, X.; Liu, S.; Zhang, H.; Zhang, S.; Meng, G.; Liu, Q.; Sun, Z.; Luo, J.; Liu, X. Polycrystalline SnSx Nanofilm Enables CO<sub>2</sub> Electroreduction to Formate with High Current Density. *Chem. Commun.* **2022**, *58*, 7654–7657.
- (49) Gao, S.; Wang, T.; Jin, M.; Zhang, S.; Liu, Q.; Hu, G.; Yang, H.; Luo, J.; Liu, X. Bifunctional Nb-N-C Atomic Catalyst for Aqueous Zn-Air Battery Driving CO<sub>2</sub> Electrolysis. *Sci. China Mater.* **2023**, *66*, 1013–1023.
- (50) Jin, Y.; Li, F.; Cui, P.; Yang, Y.; Ke, Q.; Ha, M. N.; Zhan, W.; Ruan, F.; Wan, C.; Lei, Z.; Nguyen, V. N.; Chen, W.; Tang, J. Jahn-Teller Distortion Assisted Interstitial Nitrogen Engineering: Enhanced Oxygen Dehydrogenation Activity of N-Doped Mn<sub>x</sub>Co<sub>3-x</sub>O<sub>4</sub> Hierarchical Micro-Nano Particles. *Nano Res.* **2021**, *14*, 2637–2643.
- (51) Sultan, S.; Lee, H.; Park, S.; Kim, M. M.; Yoon, A.; Choi, H.; Kong, T. H.; Koe, Y. J.; Oh, H. S.; Lee, Z.; Kim, H.; Kim, W.; Kwon, Y. Interface Rich CuO/Al<sub>2</sub>CuO<sub>4</sub> Surface for Selective Ethylene

- Production from Electrochemical CO<sub>2</sub> Conversion. *Energy Environ. Sci.* **2022**, *15*, 2397–2409.
- (52) Ma, W.; Xie, S.; Liu, T.; Fan, Q.; Ye, J.; Sun, F.; Jiang, Z.; Zhang, Q.; Cheng, J.; Wang, Y. Electrocatalytic Reduction of CO<sub>2</sub> to Ethylene and Ethanol through Hydrogen-Assisted C–C Coupling over Fluorine-Modified Copper. *Nat. Catal.* **2020**, *3*, 478–487.
- (53) Yin, Z.; Yu, C.; Zhao, Z.; Guo, X.; Shen, M.; Li, N.; Muzzio, M.; Li, J.; Liu, H.; Lin, H.; Yin, J.; Lu, G.; Su, D.; Sun, S. Cu<sub>3</sub>N Nanocubes for Selective Electrochemical Reduction of CO<sub>2</sub> to Ethylene. *Nano Lett.* **2019**, *19*, 8658–8663.
- (54) Chakraborty, S.; Das, R.; Riyaz, M.; Das, K.; Singh, A. K.; Bagchi, D.; Vinod, C. P.; Peter, S. C. Wurtzite CuGaS<sub>2</sub> with an In-Situ-Formed CuO Layer Photocatalyzes CO<sub>2</sub> Conversion to Ethylene with High Selectivity. *Angew. Chem., Int. Ed.* **2023**, *62*, No. e202216613.
- (55) Chang, X.; Li, J.; Xiong, H.; Zhang, H.; Xu, Y.; Xiao, H.; Lu, Q.; Xu, B. C–C Coupling Is Unlikely to Be the Rate-Determining Step in the Formation of C<sub>2+</sub> Products in the Copper-Catalyzed Electrochemical Reduction of CO. *Angew. Chem., Int. Ed.* **2022**, *61*, No. e202111167.
- (56) de Luna, P.; Quintero-Bermudez, R.; Dinh, C. T.; Ross, M. B.; Bushuyev, O. S.; Todorović, P.; Regier, T.; Kelley, S. O.; Yang, P.; Sargent, E. H. Catalyst Electro-Redeposition Controls Morphology and Oxidation State for Selective Carbon Dioxide Reduction. *Nat. Catal.* **2018**, *1*, 103–110.
- (57) Kim, J.; Choi, W.; Park, J. W.; Kim, C.; Kim, M.; Song, H. Branched Copper Oxide Nanoparticles Induce Highly Selective Ethylene Production by Electrochemical Carbon Dioxide Reduction. *J. Am. Chem. Soc.* **2019**, *141*, 6986–6994.
- (58) Li, M.; Ma, Y.; Chen, J.; Lawrence, R.; Luo, W.; Sacchi, M.; Jiang, W.; Yang, J. Residual Chlorine Induced Cationic Active Species on a Porous Copper Electrocatalyst for Highly Stable Electrochemical CO<sub>2</sub> Reduction to C<sub>2+</sub>. *Angew. Chem., Int. Ed.* **2021**, *60*, 11487–11493.
- (59) Mistry, H.; Varela, A. S.; Bonifacio, C. S.; Zegkinoglou, I.; Sinev, I.; Choi, Y. W.; Kisslinger, K.; Stach, E. A.; Yang, J. C.; Strasser, P.; Cuenya, B. R. Highly Selective Plasma-Activated Copper Catalysts for Carbon Dioxide Reduction to Ethylene. *Nat. Commun.* **2016**, *7*, No. 12123.
- (60) Zhang, W.; Huang, C.; Zhu, J.; Zhou, Q.; Yu, R.; Wang, Y.; An, P.; Zhang, J.; Qiu, M.; Zhou, L.; Mai, L.; Yi, Z.; Yu, Y. Dynamic Restructuring of Coordinatively Unsaturated Copper Paddle Wheel Clusters to Boost Electrochemical CO<sub>2</sub> Reduction to Hydrocarbons. *Angew. Chem., Int. Ed.* **2022**, *61*, No. e202112116.
- (61) Liang, Z. Q.; Zhuang, T. T.; Seifitokaldani, A.; Li, J.; Huang, C. W.; Tan, C. S.; Li, Y.; de Luna, P.; Dinh, C. T.; Hu, Y.; Xiao, Q.; Hsieh, P. L.; Wang, Y.; Li, F.; Quintero-Bermudez, R.; Zhou, Y.; Chen, P.; Pang, Y.; Lo, S. C.; Chen, L. J.; Tan, H.; Xu, Z.; Zhao, S.; Sinton, D.; Sargent, E. H. Copper-on-Nitride Enhances the Stable Electrosynthesis of Multi-Carbon Products from CO<sub>2</sub>. *Nat. Commun.* **2018**, *9*, No. 3828.
- (62) Yin, Z.; Yu, C.; Zhao, Z.; Guo, X.; Shen, M.; Li, N.; Muzzio, M.; Li, J.; Liu, H.; Lin, H.; Yin, J.; Lu, G.; Su, D.; Sun, S. Cu<sub>3</sub>N Nanocubes for Selective Electrochemical Reduction of CO<sub>2</sub> to Ethylene. *Nano Lett.* **2019**, *19*, 8658–8663.
- (63) Brisard, G. M.; Zenati, E.; Gasteiger, H. A.; Markovic, N. M.; Ross, P. N. Underpotential Deposition of Lead on Copper (111): A Study Using a Single-Crystal Rotating Ring Disk Electrode and Ex Situ Low-Energy Electron Diffraction and Auger Electron Spectroscopy. *Langmuir* **1995**, *11*, 2221–2230.
- (64) Herrero, E.; Buller, L. J.; Abruña, H. D. Underpotential Deposition at Single Crystal Surfaces of Au, Pt, Ag and Other Materials. *Chem. Rev.* **2001**, *101*, 1897–1930.
- (65) Sebastián-Pascual, P.; Escudero-Escribano, M. Surface Characterization of Copper Electrocatalysts by Lead Underpotential Deposition. *J. Electroanal. Chem.* **2021**, *896*, No. 115446.
- (66) Hammer, B.; Hansen, L. B.; Nørskov, J. K. Improved Adsorption Energetics within Density-Functional Theory Using Revised Perdew-Burke-Ernzerhof Functionals. *Phys. Rev. B: Condens. Matter Mater. Phys.* **1999**, *59*, 7413–7421.
- (67) Blöchl, P. E. Projector Augmented-Wave Method. *Phys Rev B* **1994**, *50*, 17953–17979.
- (68) Grimme, S.; Antony, J.; Ehrlich, S.; Krieg, H. A Consistent and Accurate Ab Initio Parametrization of Density Functional Dispersion Correction (DFT-D) for the 94 Elements H–Pu. *J. Chem. Phys.* **2010**, *132*, No. 154104.

## □ Recommended by ACS

### Hydrophobic, Ultrastable Cu<sup>δ+</sup> for Robust CO<sub>2</sub> Electroreduction to C<sub>2</sub> Products at Ampere-Current Levels

Mingwei Fang, Lei Jiang, et al.

MAY 11, 2023

JOURNAL OF THE AMERICAN CHEMICAL SOCIETY

READ ▶

### Nanograin-Boundary-Abundant Cu<sub>2</sub>O-Cu Nanocubes with High C<sub>2+</sub> Selectivity and Good Stability during Electrochemical CO<sub>2</sub> Reduction at a Current Density of 5...

Qiqi Wu, Guangxu Chen, et al.

JUNE 20, 2023

ACS NANO

READ ▶

### Efficient CO Electroreduction to Methanol by CuRh Alloys with Isolated Rh Sites

Junbo Zhang, Gengfeng Zheng, et al.

MAY 11, 2023

ACS CATALYSIS

READ ▶

### Interfacial Synergy between the Cu Atomic Layer and CeO<sub>2</sub> Promotes CO Electrocoupling to Acetate

Tang Yang, Xiaoqing Huang, et al.

APRIL 27, 2023

ACS NANO

READ ▶

Get More Suggestions >